nature communications

Article

https://doi.org/10.1038/s41467-025-58255-x

Taking three-dimensional x-ray diffraction (3DXRD) from the synchrotron to the laboratory scale

Received: 27 June 2024

Accepted: 12 March 2025

Published online: 29 April 2025

Check for updates

Seunghee Oh[1,4] ✉, Yuefeng Jin[1], Sangwon Lee[1], Wenxi Li[1,2], Ken Geauvreau[3], Matthew Williams[3], Robert Drake[3] & Ashley Bucsek[1,2] ✉

Three-dimensional x-ray diffraction (3DXRD), a rotating x-ray diffraction technique, is a powerful tool for studying the micromechanical behavior of polycrystalline materials, capable of measuring the volume, position, orientation, and strain of thousands of grains simultaneously. However, its application has been historically limited to synchrotron facilities. Here, we present the first demonstration of laboratory-scale 3DXRD (Lab-3DXRD) using a liquid-metal-jet source. Lab-3DXRD achieves accuracy comparable to synchrotron-based 3DXRD, as validated against laboratory diffraction contrast tomography (LabDCT) and synchrotron-3DXRD. Over 96% of the grains detected with Lab-3DXRD are cross-validated, particularly for coarse grains (> ~60 μm), while the results suggest that finer grains should be accessible by taking advantage of high-efficiency detectors. We further demonstrate that its sensitivity to finer grains is enhanced by incorporating pre-characterization into the analysis. This study establishes Lab-3DXRD as a practical alternative to synchrotron techniques, making 3DXRD accessible to a wider range of academic and industrial researchers.

Over the past two decades, modern synchrotron x-ray characterization techniques have revolutionized contemporary materials science. Researchers can now watch how microstructures evolve under environmental stimuli in situ, in 3D, and across several orders of magnitude in length scale. These measurements are opening new doors into our understanding of structural, functional, and geological materials via direct observation. Three-dimensional x-ray diffraction (3DXRD) is a preeminent example. 3DXRD, alternatively called high-energy diffraction microscopy (HEDM) or high-energy x-ray microscopy (HEXM), is a rotating x-ray diffraction technique that can be used to measure the relative volume, position, crystallographic orientation, and strain state of each individual crystal or grain, for up to tens of thousands of grains concurrently. For this reason, 3DXRD is perhaps the most powerful tool we have for understanding the micromechanical behavior of polycrystalline materials.

Since its advent, 3DXRD has been used to understand a wide diversity of material processes and mechanical behaviors, including recrystallization and grain growth[1–6], crystal plasticity[1,7–12], twinning and phase transformations[13–17], fatigue[18–22], fracture[21,23–26], and beyond[5,27–31]. This list is in no way exhaustive, as the number of works utilizing 3DXRD (or HEDM) has increased exponentially since its invention in the early 2000s. The escalation from 25 citations in 2011 to 1,145 citations in 2023, according to Clarivate's journal citation reports[32], reflects 3DXRD's widespread acceptance and integration into research methodologies.

The principals of 3DXRD are as follows: A sample volume is illuminated by a monochromatic box or line-focused x-ray beam while diffraction patterns are serially recorded during a 360° sample rotation. There are two main versions of 3DXRD: a near-field version and a far-field version (see also: point-focused or scanning versions[33–35]). Only the

[1]Department of Mechanical Engineering, University of Michigan, Ann Arbor, MI 48109, USA. [2]Department of Materials Science and Engineering, University of Michigan, Ann Arbor, MI 48109, USA. [3]PROTO Manufacturing Ltd, Windsor, ON N9J 3W3, Canada. [4]Present address: X-ray Science Division, Argonne National Laboratory, Lemont, IL 60439, USA. ✉e-mail: saoh5@anl.gov; abucsek@umich.edu

far-field version is used to routinely measure grain elastic strain states, which (knowing the stiffness tensor) can then be used to measure grain stress states. Specifically, the far-field version of 3DXRD can be used to measure the grain centroid, relative grain volume, grain-averaged crystallographic orientation, and grain-averaged elastic strain tensor with resolutions typically quoted as 10 μm (spatial), 0.1° (orientation), and 10^{-4} (strain)[36]. These measurements can be converted to microstructures using a weighted Voronoi tessellation (see, e.g., Neper[37]). Multiple software packages including MIDAS[38], HEXRD[39], and ImageD11[40] are available for data analysis. Researchers have also developed specialized analysis tools to measure other types of grain-specific information from 3DXRD measurements, including dislocation density[17,41], slip system activation[12,18,42], orientation spread[43], deformation twinning[44], martensitic phase transformations[45], and beyond. All of this information is contained within the richness of 3DXRD data sets.

Despite its numerous and considerable advantages, the accessibility of 3DXRD remains limited to a small number of storage-ring-based x-ray radiation source facilities. Dedicated HEDM beamlines can be found at the Advanced Photon Source (APS) at Argonne National Laboratory and the Cornell High Energy Synchrotron Source (CHESS) in the U.S., the European Synchrotron Radiation Facility (ESRF) in France, Petra-III in Germany, and SPring-8 in Japan. To access these facilities, users can submit proposals for a maximum of six days per visit that are reviewed and scored by a panel. The 1-ID beamline, for example, is one of, if not the most, oversubscribed beamline at the APS. While this speaks to the popularity of synchrotron-based 3DXRD, there is a significant barrier for those who may be unfamiliar with the user facility proposal process, and even expert users need to wait months or even years for a single experiment. Beyond these facilities, there is currently no alternative to the strain-mapping, far-field version of 3DXRD (using, e.g., electron-based methods). Consequently, the limited access to 3DXRD constrains the research applications and dissemination of this distinctive and powerful technique.

The accessibility of instrumentation is critical for expanding to new research areas, e.g., the diverse application of benchtop x-ray diffractometers[46–48]. Consequently, there have been concerted efforts to bring advanced characterization techniques from synchrotron facilities into standard laboratories. One relevant example is diffraction contrast tomography (DCT). Once exclusive to synchrotrons, laboratory-scale DCT (LabDCT) has now become a popular technique for studying the 3D grain maps of polycrystalline materials[49–51]. Ongoing technological advancements in x-ray sources and detectors and user-friendly analysis software packages have facilitated the commercialization of DCT[52,53]. Although LabDCT has some limitations (e.g., the degree of deformation), this invention has increased accessibility for a broader range of users and is now being employed across various research industries[54–56]. Another example is small-angle x-ray scattering (SAXS). With advancements to brightness and stability in synchrotron radiation that began in the 1970s, SAXS was developed and refined at synchrotron facilities[57–59], and more recent improvements in x-ray optics and other instruments have since made SAXS available in laboratory settings[60–63]. Although laboratory SAXS has some trade-offs compared to synchrotron SAXS, these developments have significantly enhanced the growth of research utilizing SAXS[61,64].

In this work, we bring the far-field version of 3DXRD from the synchrotron to the laboratory scale for the first time, demonstrating that researchers can access these measurements in their home institutions in a way that was not previously possible. We present the first-ever laboratory-scale 3DXRD (Lab-3DXRD) microscope. We share the results of a comparative benchmarking validation study of Lab-3DXRD against synchrotron 3DXRD at CHESS and LabDCT. The results show that the position, orientation, and strain capabilities of Lab-3DXRD are comparable to those of synchrotron-based 3DXRD. While our current detector (a Varex XRD1611-xP) can be used to reliably and accurately measure coarse (> ~60 μm) grains, this limit is detector-dependent, and finer grains should be accessible by taking advantage of high-efficiency detectors (e.g., photon-counting detectors). We also demonstrate how the detection of fine grains can be improved by seeding the analysis with grains pre-characterized by complementary techniques like LabDCT. Finally, we discuss the outlook for Lab-3DXRD to supplement 3DXRD's growing user base as well as reach new untapped scientific communities.

Results and discussion

Overview of the lab-3DXRD, synch-3DXRD, and labDCT measurements

An overview of the 3D grain information measured using Lab-3DXRD, synchrotron-based 3DXRD (referred to here as "Synch-3DXRD"), and LabDCT is provided in Fig. 1. This result provides a first look at the performance of Lab-3DXRD compared against Synch-3DXRD and LabDCT. As mentioned in the previous section, the results shown here and discussed throughout the rest of the manuscript correspond only to grains observed within the ~$1 \times 1 \times 1$ mm^3 sample volume that is common to all three measurements. These grains are opaque in Fig. 1a-c. The partially transparent grains in Fig. 1b,c correspond to grains that are outside of this volume (i.e., grains that are not included in the validation study).

In the grain 3D maps (Fig. 1a–c), the grains within all three volumes nominally occupy similar positions. By comparison, the LabDCT grain map shows a higher count of relatively small grains than that of Lab-3DXRD or Synch-3DXRD. This result is representative of a common theme that will be discussed throughout this work, i.e., that: (1) Lab-3DXRD results are consistent with Synch-3DXRD and LabDCT for moderate-to-large-sized grains, and (2) Lab-3DXRD is less robust detecting finer grains, though this grain size limitation is expected to be largely detector-dependent. The largest grain, located at the bottom of the reconstructed volume in the LabDCT dataset (Fig. 1c), is absent in the 3DXRD results (Fig. 1a, b). This absence is likely due to saturated Bragg reflections, which are automatically excluded from the 3DXRD analysis.

In the inverse pole figure (IPF) orientation maps (Fig. 1d–f), all three techniques provide similar orientation measurements, demonstrating the ability of Lab-3DXRD to measure grain orientations as well as Synch-3DXRD or LabDCT (discussed more in the next section). Figure 1g–i shows the grain size distributions for the three measurements. The relative grain volume in LabDCT was calculated from the ratio of voxels forming a grain to the total voxel count in the reconstructed volume, whereas the relative grain volume in Lab-3DXRD and Synch-3DXRD were calculated from the relative diffraction peak intensities as described in the "Methods" section. The relative grain volumes show similar distributions across all three techniques. The equivalent elastic strains (Fig. 1j, k) measured using Lab-3DXRD versus Synch-3DXRD show good agreement. (As a reminder, LabDCT cannot be used to measure strains.) Altogether, the results show that Lab-3DXRD can be used to measure grain orientations and elastic strains as accurately as Synch-3DXRD, discussed more quantitatively in the following sections. On the other hand, Synch-3DXRD has higher completeness values (Fig. 1l–n) than that of either laboratory-scale technique. Completeness is defined as the number of measured diffraction peaks in proportion to the number of expected diffraction peaks for a given grain. The higher completeness observed with Synch-3DXRD likely reflects the greater brilliance and consequently higher signal-to-noise ratios characteristic of synchrotron-based sources. This result speaks to the main challenge for Lab-3DXRD and for laboratory x-ray source techniques in general, i.e., low signal-to-noise ratios.

Analysis of grains paired across lab-3DXRD, synch-3DXRD, and labDCT measurements

To cross-validate Lab-3DXRD against Synch-3DXRD and LabDCT, we performed grain pairing where we identified grains that were detected

https://doi.org/10.1038/s41467-025-58255-x

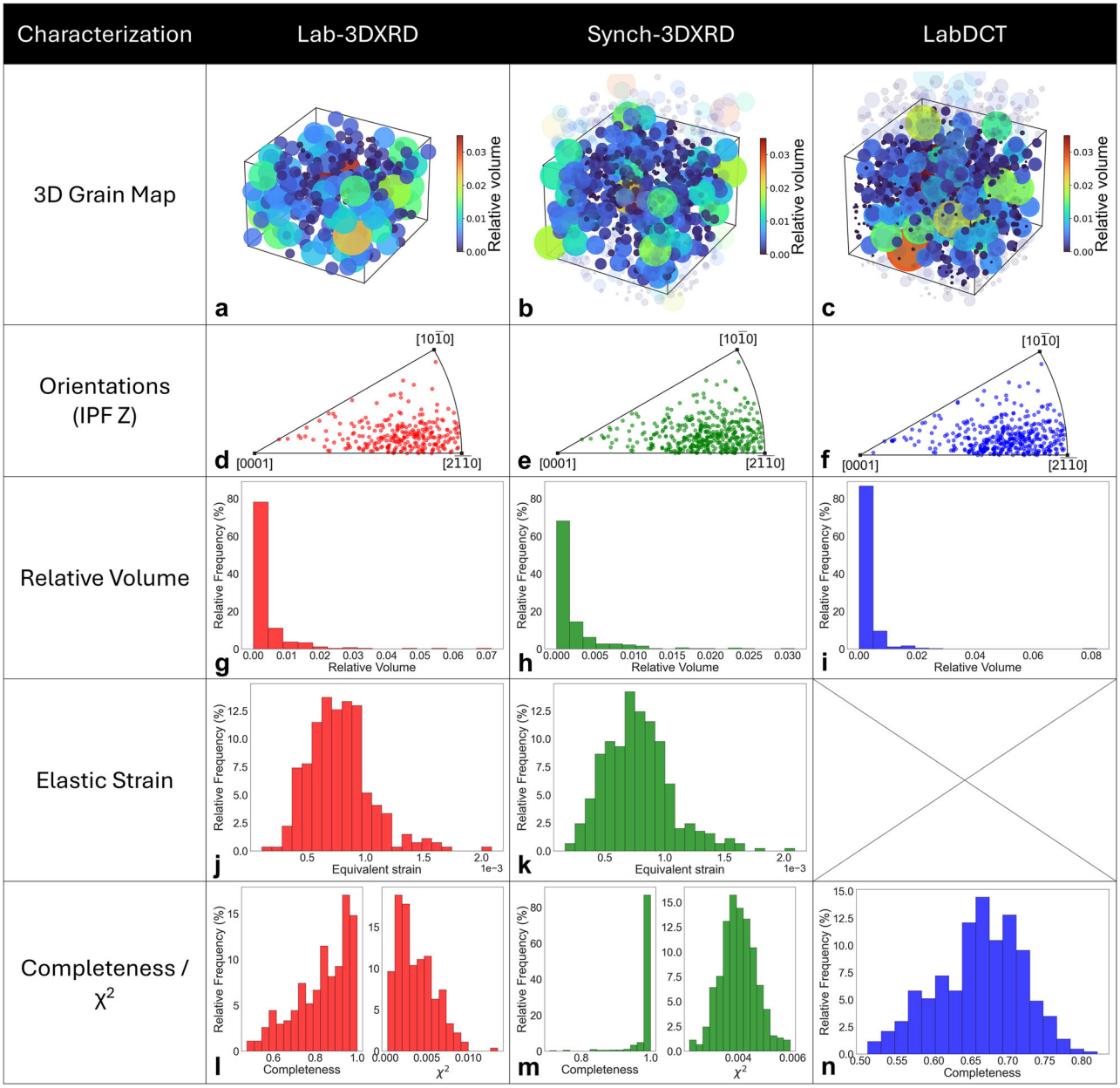

Fig. 1 | Overview of the 3D grain information measured obtained from laboratory-scale 3DXRD (Lab-3DXRD), synchrotron-based 3DXRD (Synch-3DXRD), and laboratory diffraction contrast tomography (LabDCT). a–c Grain positions where marker size and color both correspond to relative grain volume; **d–f** Grain orientations shown in an inverse pole figure (IPF); **g–i** Relative grain volumes; **j, k** Grain strains; **l–n** Grain completeness and goodness of fit (χ^2). Note: Goodness of fit is only reported for the two 3DXRD measurements and is not available from the LabDCT reconstruction software.

across each pair of techniques, i.e., grains that were found in both the Lab-3DXRD and LabDCT data sets ("Lab-3DXRD / LabDCT"), grains that were found in both the Lab-3DXRD and Synch-3DXRD data sets ("Lab-3DXRD / Synch-3DXRD"), and grains that were found in both the LabDCT and Synch-3DXRD data sets ("LabDCT / Synch-3DXRD"). Using a first criterion of <0.25° misorientation, we found 258 grain pairs between Lab-3DXRD and LabDCT, 257 grain pairs between Lab-3DXRD and Synch-3DXRD, and 363 grain pairs between Synch-3DXRD and LabDCT (Fig. 2a). Of the 270 grains detected with Lab-3DXRD, only 12 were not identified in the LabDCT result and 13 were not identified in the Synch-3DXRD result. After identifying grain pairs based on orientation, a second criterion was enforced based on grain centroid position using a maximum distance of 0.2 mm. After this second criterion, we found 256 grain pairs between Lab-3DXRD and LabDCT and 253 grain pairs between Lab-3DXRD and Synch-3DXRD (Fig. 2a).

Although Lab-3DXRD measured fewer grains than Synch-3DXRD or LabDCT, a significantly higher percentage of the Lab-3DXRD grains were validated by one or both other techniques (96% for Lab-3DXRD / LabDCT and 94% for Lab-3DXRD / Synch-3DXRD, compared to 70% for Synch-3DXRD / LabDCT). Even though both Synch-3DXRD and LabDCT found between 430 and 450 grains, only 310 of these grains could be identified in the other data set. Even without a position criterion (i.e., enforcing only the misorientation criterion of 0.25°), only 363 grains could be paired between Synch-3DXRD and LabDCT. This may speak to inherent differences between the way that grain orientations are measured between 3DXRD and LabDCT, leading to some discrepancies above our threshold criterion of 0.25°. It may also suggest that the orientations and positions of very small grains cannot be measured with high precision using either Synch-3DXRD or LabDCT. Also, a few large grains in the slices are not characterized by both

https://doi.org/10.1038/s41467-025-58255-x

Techniques	Lab-3DXRD	Synch-3DXRD	LabDCT
Detected grains	270	451	430

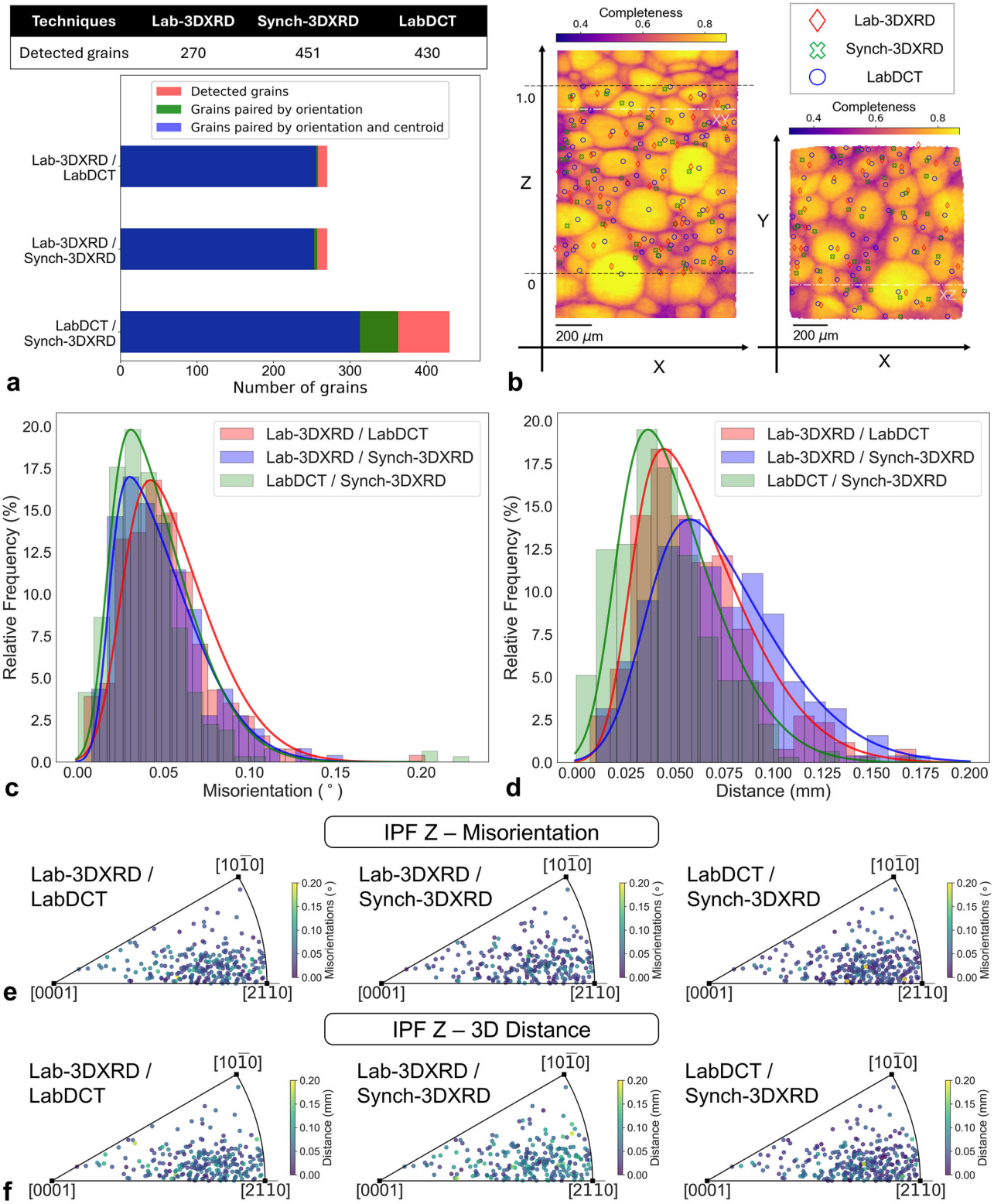

Fig. 2 | Overview of grains pairing across laboratory-scale 3DXRD (Lab-3DXRD), synchrotron-based 3DXRD (Synch-3DXRD), and laboratory diffraction contrast tomography (LabDCT). a The number of grains detected and paired across each technique combination; **b** 2D orthogonal XZ and XY "slices" of the LabDCT reconstruction (color = completeness), marked by a white dot line in each slice with markers indicating grain centroids measured by each technique; **c** Distribution of misorientation measured between grains paired across LabDCT and Lab-3DXRD (red), Lab-3DXRD and Synch-3DXRD (blue), and LabDCT and Synch-3DXRD (green); **d** Distribution of distance measured between grains paired across LabDCT and Lab-3DXRD (red), Lab-3DXRD and Synch-3DXRD (blue), and LabDCT and Synch-3DXRD (green); **e** IPF (Z) map colored by misorientations; **f** IPF (Z) map colored by centroid distances.

https://doi.org/10.1038/s41467-025-58255-x

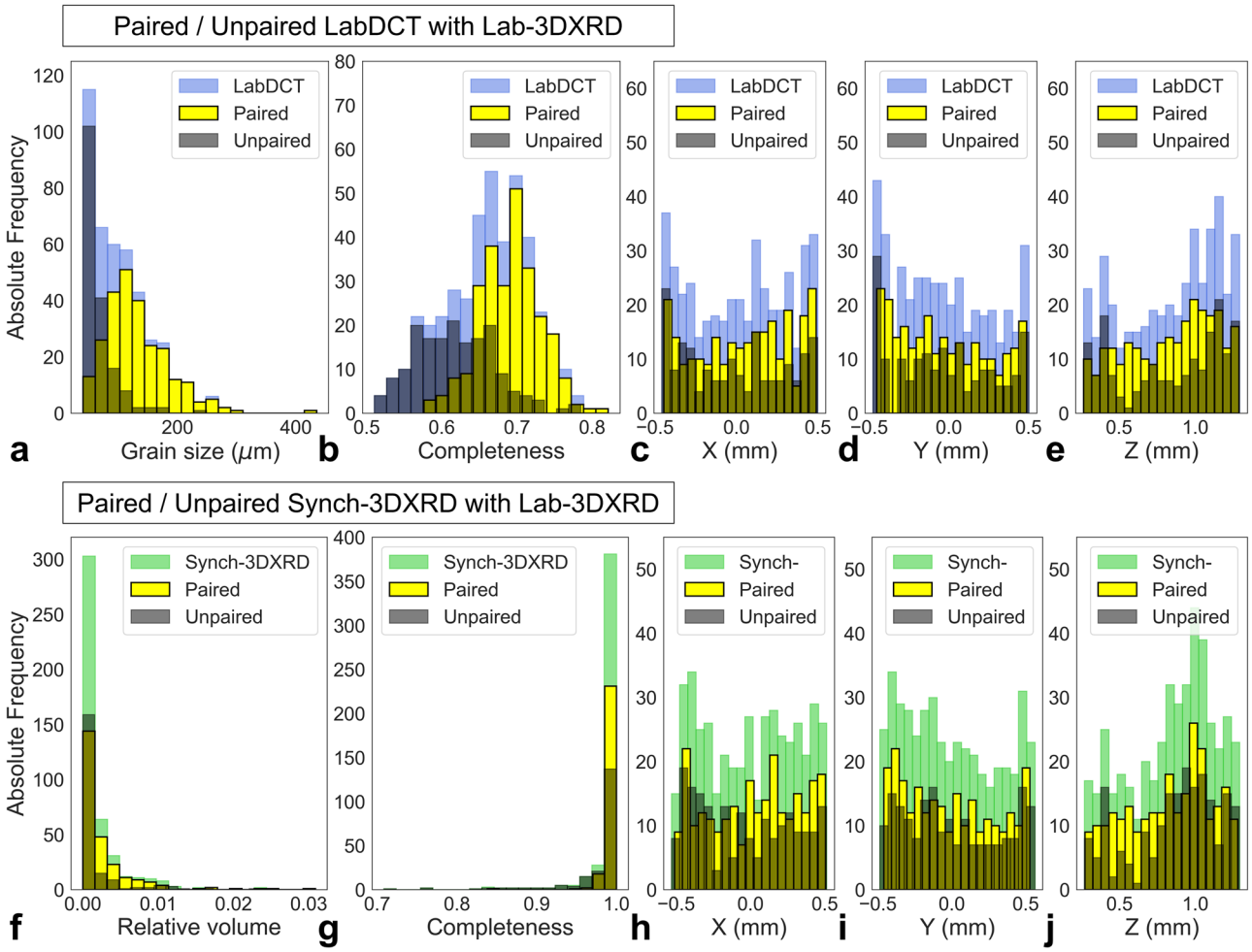

Fig. 3 | Comparison of paired vs. unpaired from the analyzed grains of laboratory diffraction contrast tomography (LabDCT) and synchrotron-based 3DXRD (Synch-3DXRD) grains compared with laboratory-scale 3DXRD (Lab-3DXRD). Paired and unpaired grains of LabDCT with respect to (**a**) Grain size measured by LabDCT; **b** Completeness measured by LabDCT; **c**–**e** Grain centroid position measured by LabDCT; Paired and unpaired grains of Synch-3DXRD with respect to (**f**) Relative volume measured by Synch-3DXRD; **g** Completeness measured by Synch-3DXRD; **h**–**j** Grain centroid position measured by Synch-3DXRD.

3DXRD techniques, likely due to saturated Bragg reflections that are automatically excluded from the analysis.

The misorientation values between grain pairs are shown in Fig. 2c. The distribution peak values are 0.042° for Lab-3DXRD / LabDCT grain pairs, 0.030° for Lab-3DXRD / Synch-3DXRD grain pairs, and 0.031° for Synch-3DXRD / LabDCT grain pairs. Note that all three values are less than the 0.1° orientation resolution typically reported for far-field 3DXRD[36,65]. Also, note that the lowest misorientation is found in the grain pairs for Lab-3DXRD / Synch-3DXRD, indicating that the Lab-3DXRD orientation measurements are closest to those measured with Synch-3DXRD, even closer than LabDCT to Synch-3DXRD. In Fig. 2e, the orientations are shown with respect to the misorientation values, showing that there is no correlation between grain orientation and misorientation and thus no artifacts that might affect the orientation measurements for specific orientations. Overall, these findings affirm the ability of Lab-3DXRD to measure grain orientations with accuracies that are comparable to that of Synch-3DXRD.

The centroid position differences between grain pairs are shown in Fig. 2d. The distribution peak position values are 44 μm for Lab-3DXRD / LabDCT pairs, 58 μm for Lab-3DXRD / Synch-3DXRD pairs, and 36 μm for Synch-3DXRD / LabDCT pairs. The paired grains in Synch-3DXRD / LabDCT are predominantly within 0.1 mm, a reasonable outcome based the average grain size (104.3 μm) and on the reported spatial resolutions[36,52,54]. The paired grains with Lab-3DXRD exhibit a slightly broader distribution skewing toward higher distances. Overall, these findings suggest the accuracy of Lab-3DXRD in determining grain position is slightly lower than that of Synch-3DXRD, likely due to the signal-to-noise ratio. Of the quantities that 3DXRD is used to measure (i.e., position, orientation, strain, and relative volume), the grain centroids are measured with the smallest degree of accuracy since the position-related deviations in diffraction peak locations are significantly smaller than orientation-related or strain-related deviations (in the far-field geometry)[36]. This explains why Lab-3DXRD is comparable to Synch-3DXRD in terms of grain orientations (Figs. 1d, e and 2c) and strains (Fig. 1j, k), but it is slightly less accurate than Synch-3DXRD and LabDCT in terms of grain positions (Fig. 2d). This also points to opportunities for improving position accuracy with Lab-3DXRD using a more sensitive detector.

Characteristics of “paired” versus “unpaired” grains

Figure 3 shows the grain sizes, completeness values, and 3D centroids (x, y, z coordinates) for the LabDCT grains (Fig. 3a–e) and Synch-3DXRD grains (Fig. 3f–j) that were paired vs. not paired (“unpaired”) with Lab-3DXRD. The numbers of unpaired grains in the LabDCT and Synch-3DXRD datasets are 172 and 194, respectively, while the numbers of paired grains are 258 and 257. Figure 3a shows that grains with a variety of sizes were measured with Lab-3DXRD and confirmed with LabDCT, and the majority of unpaired LabDCT grains were small (less than ~55 μm). The average grain size measured by LabDCT is 104.3 μm, and the average size is 130.9 μm for paired grains and 65.1 μm for

unpaired grains. The difficulty of detecting small grains with Lab-3DXRD is due to the fact that small grains have lower completeness values. Completeness is the ratio of the number of detected diffraction peaks to the number of expected diffraction peaks for a given grain. Since small grains have low-intensity diffraction peaks that may not be detected above the background noise level, small grains also tend to have lower completeness values. The average LabDCT completeness value is 0.7 for paired grains and 0.6 for unpaired grains (Fig. 3b). Similarly, in the Synch-3DXRD grains (Fig. 3g), the completeness of paired grains with Lab-3DXRD is primarily concentrated around 1.0, whereas unpaired grains are distributed across a lower completeness range. Overall, these results speak to the main challenge associated with Lab-3DXRD, i.e., the low signal-to-noise ratio, which makes it difficult to confidently detect small grains. Longer exposure times or detector binning can be explored to enhance the signal-to-noise ratio, and the use of a more sensitive (e.g., photon-counting) detector is expected to significantly improve the signal-to-noise ratio and thus the ability to detect small grains.

While grain size is the most dominant factor influencing Lab-3DXRD's ability to characterize a grain, the location of the grain may also have a small influence in this particular experiment. Figure 3c–e shows the centroid locations of the paired vs. unpaired LabDCT grains compared to Lab-3DXRD. The extremes of the x, y, and z-coordinates correspond to the edges of the incident beam. Notice that the number of unpaired grains at the beam edges are slightly higher than the center of the beam. This may be due to the fact that the incident beam intensity is slightly lower at the beam edges, in addition to the fact that the size of the beam (1.05×1.05 mm^2, measured via the FWHM of the incident beam intensity; see Supplementary Fig. S1c, d) is very close to the size of the specimen cross-section. Thus, our results could be improved by using a slightly larger beam, or a slightly smaller specimen.

Evaluation of Lab-3DXRD through correlation analysis

A comprehensive investigation of Lab-3DXRD's capabilities was performed by analyzing correlations between various parameters of paired grains, as detailed in Supplementary Figs. S5 and S6. The strongest correlations were observed with completeness. Generally, completeness increases with grain size, as larger grains diffract x-rays more intensely than smaller grains, thereby exceeding the detector noise threshold more easily[17,26,66]. The scatter plot in Fig. 4 shows that completeness is exponentially proportional to grain size. This relationship offers insight into determining a grain size limit that Lab-3DXRD can reconstruct. From the paired grains between Lab-3DXRD and LabDCT, the minimum grain size is 40.2 µm, but this size may misrepresent the actual size limit of the Lab-3DXRD. In Fig. 3a, most unpaired grains fall within the 40 µm to 110 µm range, while only a small fraction of paired grains are within this size range. So, to ascertain the size limit, the data points of grain size with Lab-3DXRD's completeness are fitted by an exponential relation, resulting in a fitting curve (a dashed curve in Fig. 4) converging at 63.9 µm with decreasing completeness. Therefore, assuming that grain size is the sole component affecting completeness in the experimental setup[26,66], 63.9 µm can be thought of as a rough size limit of Lab-3DXRD (with this particular source and detector setup). This is consistent with the fact that 240 out of 256 paired Lab-3DXRD grains are larger than 63.9 µm (although the smallest grain detected with Lab-3DXRD was 40.1 µm).

Improving lab-3DXRD using a seeded analysis strategy

The results presented above validate the capabilities of our Lab-3DXRD system in terms of grain volumes, orientations, strains, and positions. While Lab-3DXRD performs well for coarse grains, Lab-3DXRD is not as sensitive to small (< ~60 µm) grains. As discussed above, the limitation is due to low signal-to-noise ratios in our current source and detector setup and could be greatly improved by incorporating a more sensitive, e.g., photon-counting, detector. Here, we explore another means to improve the Lab-3DXRD grain tracking results (without any hardware upgrades) by seeding the 3DXRD analysis with grain orientations measured with LabDCT. This strategy is an option in cases where pre-characterization of the grain structure is available using DCT, the near-field version of 3DXRD/HEDM, or (for thin samples) electron backscatter diffraction (EBSD).

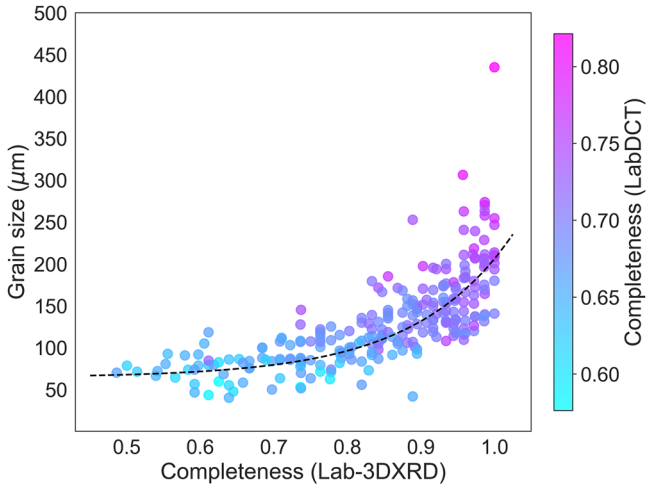

Fig. 4 | Correlation between grain size and completeness. Scatter plot of completeness (laboratory-scale 3DXRD (Lab-3DXRD)) versus grain size, colored by completeness (laboratory diffraction contrast tomography (LabDCT)), with an exponential fitting curve (dashed line).

Our approach is specific to HEXRD but can be adopted for any 3DXRD analysis software package. The far-field 3DXRD analysis in HEXRD consists of two main steps: (1) identifying grain orientations ("grain indexing"), and (2) fitting the elastic strain tensor and position of the grain based on the grain's measured diffraction peaks ("grain fitting"). With the grain seeding approach, we skip the grain indexing step and instead pass a predetermined list of grain orientations, in this case, the grain orientations measured using LabDCT.

The seeded analysis produced 42 new Lab-3DXRD grains that could be paired with LabDCT grains (using the same criteria of less than 0.25° orientation difference and less than 0.2 mm position difference), representing an improvement of 16.4 %. Figure 5 compares the Lab-3DXRD / LabDCT grain pairs found using the standard ("unseeded") analysis vs. grain pairs that are only found when using the new ("seeded") analysis. Notice that the new ("seeded") analysis resulted in the detection of grains that are significantly smaller than the grains found in the original "unseeded" analysis. The average grain size in the "Only seeded Lab-3DXRD" category is 84.04 µm (vs. 130.9 µm in the "unseeded Lab-3DXRD" category), and the smallest grain detected and verified (i.e., by pairing with LabDCT) in this category is 41.29 µm. These additionally detected grains also have lower completeness values and slightly larger orientation and position differences from their paired LabDCT grains, suggesting slightly poorer accuracy compared to the grains characterized without the seed data (see Fig. 5f, g).

All of this points to the fact that smaller grains have lower intensity diffraction peaks, resulting in a decreased ability to measure them as accurately as large grains. With our current x-ray source and detector (an indirect flat panel x-ray detector), the signal-to-noise ratio is best suited for the study of grains larger than ~60 µm in diameter. However, this work shows that the detection of small grains can be improved by seeding the far-field 3DXRD analysis, although this method necessitates prior characterization using another advanced laboratory-scale instrument. The seed method may be particularly helpful when indexing orientations associated with small volumes such as twin

https://doi.org/10.1038/s41467-025-58255-x

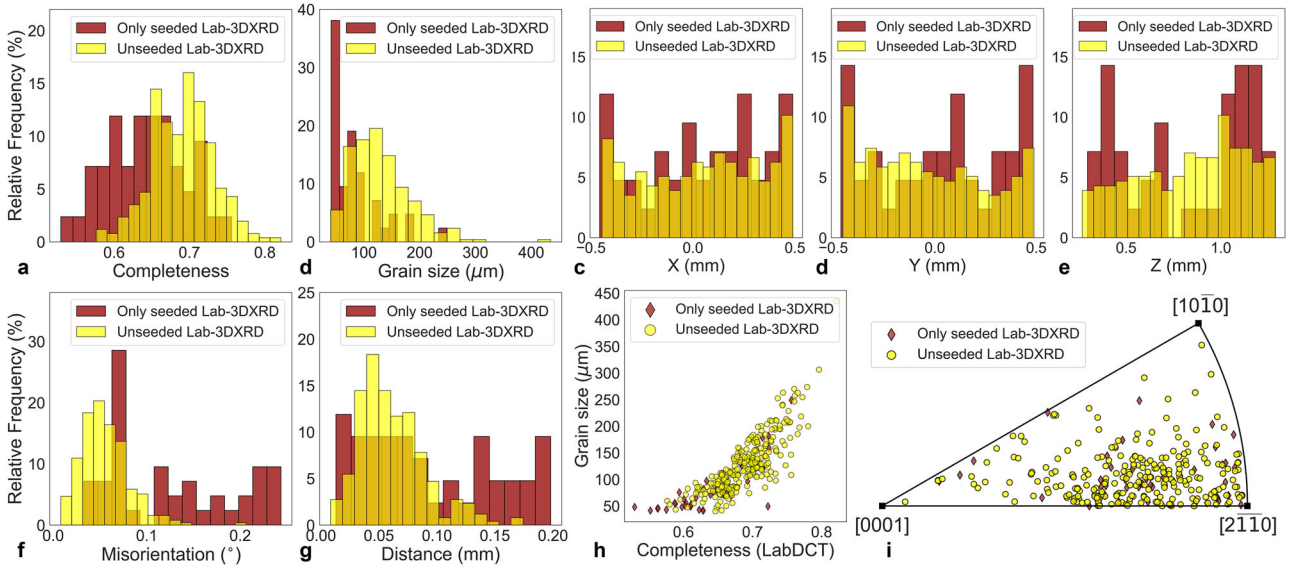

Fig. 5 | Comparison of paired laboratory-scale 3DXRD (Lab-3DXRD)/ laboratory diffraction contrast tomography (LabDCT) grains measured using the standard analysis ("Unseeded Lab-3DXRD," yellow) and the new paired grains measured using the seeded analysis ("Only seeded Lab-3DXRD," red). **a** Completeness measured by LabDCT; **b** Grain size measured by LabDCT; **c**–**e** Grain position measured by LabDCT; **f** Misorientation between Lab-3DXRD and LabDCT grain pairs; **g** Distance between Lab-3DXRD and LabDCT grain pairs; **h** Completeness (Lab-3DXRD) vs. grain size (LabDCT); **i** Grain orientations (IPF direction: Z).

formation[67] and phase transformation[16]. We also expect that modifications to the measurement procedures (e.g., increasing the exposure time, binning pixels, taking multiple images per rotation increment, and incorporating additional preprocessing steps), can be tested to enhance the capabilities of lab-3DXRD, as similar advancements have been actively pursued in other established techniques[68–70]. Of course, the biggest improvement that can be made is to increase the signal-to-noise ratio using a more sensitive detector from readily available technologies (e.g., photon-counting). We expect that this can lead to significant and immediate improvements in terms of the detection of fine grains.

In this work, we introduce the Lab-3DXRD microscope, demonstrate its ability to measure grain-specific 3DXRD quantities (position, relative volume, orientation, and strain), and cross-validate the results in a comparative benchmarking study using established grain-tracking techniques, including synchrotron-based 3DXRD and LabDCT. The results show that Lab-3DXRD can be used to detect and characterize grains with accuracies comparable to that of synchrotron-based 3DXRD. More than 96% of the grains detected with Lab-3DXRD were cross-validated with synchrotron-based 3DXRD and/or LabDCT. While our current hardware can be used to accurately measure grains greater than ~60 µm, the results suggest that finer grains will also be accessible by taking advantage of currently available high-efficiency detectors (e.g., photon-counting detectors). We also demonstrate how the sensitivity of Lab-3DXRD to fine grains can be improved by seeding the analysis with pre-characterization measurements. This first demonstration of 3DXRD is expected to enable new, diverse communities of academic and industrial researchers to harness the advantages of 3DXRD at the laboratory scale. As a highly accessible 3D grain-tracking technique compared to synchrotron methods, Lab-3DXRD can provide researchers with hands-on 3DXRD experience, advancing our understanding of crystalline materials.

Methods

Lab-3DXRD instrumentation

The custom Lab-3DXRD system was manufactured by Proto Mfg. (Supplementary Fig. S1a). This system comprises two main components: (i) the x-ray source and optics cabinet and (ii) a walk-in enclosure, or hutch. The hutch is lead-shielded and includes various safety features to ensure secure operation. The system is managed and controlled externally via two dedicated workstations.

The Lab-3DXRD system has an Excillum MetalJet E1+ liquid-metal-jet anode source. The target material is a molten ExAlloy-I2 alloy composed of 47% gallium, 37% indium, and 16% tin by weight. Heater jackets are incorporated to maintain the flowability of the liquid alloy in its molten state. The system operates at an electron beam voltage of 160 kV and an emission current of 4.375 mA, producing a power output of 700 W. The electron beam size is adjustable and was set to 80 µm (horizontal) × 20 µm (vertical) for this study. Blooming in the vertical direction in combination with the take-off angle in the horizontal direction results in a 30-µm round apparent X-ray focal spot. The electron beam on the indium-rich target alloy produces a strong Indium Kα radiation with a brilliance of 4×10^9 photons/(s·mm²·mrad²·0.1% BW)[71,72].

A Montel x-ray optic (model AXO ASTIX + + 120) is used to collimate and monochromate the polychromatic x-rays produced by the MetalJet. This optic consists of two parabolic graded-multilayer mirrors positioned at 90° angles to each other that align and collimate the incident beam. The Montel optic also filters the energy spectrum of x-rays (Supplementary Fig. S2), producing a Kα doublet x-ray beam that includes only the Indium $K\alpha_1$ (24.21 keV) and $K\alpha_2$ (24.00 keV) peaks. The collimated beam with a divergence of 0.2 milliradians then passes through a beam shaper to change the cross-sectional dimensions of the beam. During these adjustments, the incident beam is monitored using a MiniPix TPX3 CdTe detector featuring a 256 × 256 pixel array with a pixel size of 55 µm. At the sample position, the integral intensity in the ~1.4 × 1.4 mm² x-ray beam was 1.6×10^8 counts/second. Supplementary Fig. S1d shows a profile of the photon counts along the vertical line in Supplementary Fig. S1c. This figure defines the maximum measurable layer height, which was determined to be 1.05 mm based on the full width at half maximum of the profile in Supplementary Fig. S1d. The maximum sample cross-section is dictated by the beam size: 1 × 1 mm². In addition, the x-ray attenuation and absorption of the material should be considered to determine the

https://doi.org/10.1038/s41467-025-58255-x

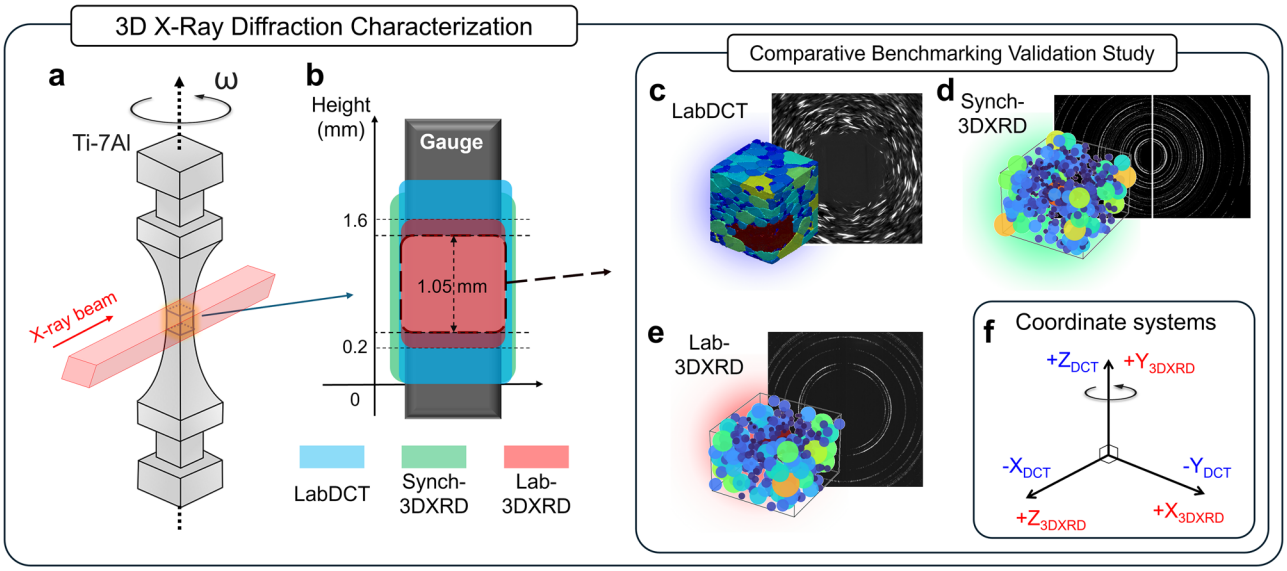

Fig. 6 | A schematic of the comparative benchmarking validation study of laboratory-scale 3DXRD. a Drawing of a Ti-7Al specimen used in this work; **b** The total sample volumes measured by each of the three techniques; **c** 3D microstructure measured with laboratory diffraction contrast tomography (LabDCT); **d** 3D scatter plot of grain centroids measured with synchrotron-based 3DXRD (Synch-3DXRD); **e** 3D scatter plot of grain centroids measured with laboratory-scale 3DXRD (Lab-3DXRD); **f** 3DXRD vs. DCT coordinate system conventions.

actual allowable sample cross-section. In this experiment, our sample (Ti-7Al with a 1×1 mm^2 cross-section) had approximately 2% transmission.

In our far-field 3DXRD setup, the sample station is mounted on a Standa 8MR190-90 motorized rotation stage (angular deviations < 40 μRa). The attached 2D translation stage facilitates movements up to 70 mm along the *x*-axis and 44 mm along the *y*-axis, as depicted in the 3DXRD coordinate system (Fig. 6f). Additionally, a separate translation stage adjusts the position of the 3DXRD detector along the *z*-axis, allowing for a sample-detector distance ranging from 195 mm to 1054 mm.

The detector is a Varex XRD1611-xP: a single amorphous silicon flat-panel detector with a CsI scintillator (84 dB dynamic range and frame rates up to 15 frames per second). Its relatively high-efficiency mapping across a wide energy range from 20 kV to 15 MV is suitable for the laboratory x-ray source in this study, even though the detection efficiency of this indirect flat-panel detector with CsI scintillator is somewhat limited around the 24 keV energy range[73–75]. The detector array consists of 4096×4096 pixels, each measuring 100×100 μm^2. The detector's active area is approximately 409.6×409.6 mm^2, offering a large coverage area for capturing diffraction patterns.

The alignment of the sample in the incident beam is performed using the MiniPix CdTe detector, and an optical camera to provide real-time monitoring of the sample's movement while the stage rotates. While the rotation axis is aligned, the CdTe detector is positioned in the path of the x-ray beam between the sample and the 3DXRD detector and is removed once alignment is completed. This setup is used to verify the position of the sample relative to the incident beam.

Material

The sample used in the validation study is an annealed Ti-7Al (Ti-7.02Al-0.11O-0.015Fe wt%) alloy with a single-phase hexagonal close-packed (HCP) crystal structure and an equiaxed microstructure with an average grain size of 100 μm. The tensile specimen was electric discharge machined into a tensile specimen with a square geometry with a cross-section of 1×1 mm^2 and a gauge length of 2 mm.

Lab-3DXRD data acquisition

Prior to the Lab-3DXRD measurements, the tilt, rotation, and center of the detector are calibrated using HEXRD[39] following the same calibration procedures for traditional synchrotron 3DXRD[76]. Specifically, detector calibration was performed using a powder x-ray diffraction pattern of a reference powder material (Si, SRM-640f) and a far-field 3DXRD measurement of ruby single crystals (SRM-1990). The sample-to-detector distance is 515 mm, allowing for complete coverage of the five inner-most Debye-Scherrer rings ({100}, {002}, {101}, {102}, and {110}) of the Ti-7Al sample. During the Lab-3DXRD measurement conducted in this study, the 3DXRD diffraction patterns are acquired over an angular (ω) interval of 0.1°with an exposure time of 2 seconds per image. Accounting for data collection process, the total measurement time for 3600 images was four hours. The acquired diffraction images undergo preprocessing, as outlined in Supplementary Figs. S3 and S4, to optimize their compatibility with the analysis software.

For the Lab-3DXRD reconstructions, we used the software package, HEXRD[39]. The analysis provides the centroid location, grain-averaged elastic strain tensor (and its equivalent elastic strain), and grain-averaged crystallographic orientation of each grain indexed within the illuminated volume through the process summarized in the Lab-3DXRD Data Preprocessing and Far-field Characterization section of the Supplementary materials. The output also includes a list of the reflections and their intensities corresponding to each grain that can be used to calculate the grain's relative volume. To ensure the accuracy of the reconstructed grains, the results are filtered using a goodness of fit (χ^2) threshold of 0.02. This goodness of fit measure is calculated by HEXRD by summing the squared residuals between the measured and predicted peak positions based on the grain's indexed orientation and fitted elastic strain and position components.

Benchmarking validation study against synchrotron 3DXRD and LabDCT

To validate the grain information measured using Lab-3DXRD, we compared the Lab-3DXRD measurements against traditional synchrotron 3DXRD (Synch-3DXRD) and LabDCT measurements on the same sample in a comparative benchmarking validation study.

The synchrotron 3DXRD measurements were conducted at the Forming and Shaping Technology (FAST) beamline located in the ID3A hutch at CHESS. The energy of the monochromatic x-rays, with a bandwidth of 6.0×10^{-4} was 23.22 keV, closely matching the energy of In $K\alpha_1$ (24.21 keV). As a third-generation synchrotron, the peak brilliance is around 10^{19} photons/(s·mm²·mrad²·0.1% BW)[77]. The collimated x-ray "box" beam was 2.0 mm (width) by 1.0 mm (height) with divergences of 0.05 milliradians (width) and 0.01 milliradians (height). The data acquisition was performed in two layers with a 0.2 mm overlap, resulting in a total measurement height of 1.8 mm (Fig. 6b). The detector array consisted of two Dexela 2923 area detectors. The sample-to-detector distance was set to 525 mm, similar to that of Lab-3DXRD. 3DXRD measurements were collected over 360° rotation at a ω interval of 0.25°. The exposure time for each collection was 0.25 seconds. The measurements were analyzed using the HEXRD package using the same procedure as that of Lab-3DXRD. To ensure the accuracy of the reconstructed grains, the results were filtered using a χ^2 threshold of 0.02 (the same criterion used for Lab-3DXRD). For Lab-3DXRD and Synch-3DXRD, the relative volumes were determined by normalizing the {101} reflection intensities of individual grains to the total summation of intensities across all detected grains[14,38]. The choice of {101} reflections is motivated by their characteristic high intensities in general HCP diffraction profiles.

The LabDCT measurements were conducted using a Zeiss Xradia Versa 520 equipped with the Flat Panel Extension (FPX). The special FPX option includes a larger (3072 × 1944 pixel) detector than the standard instrument package. The laboratory x-ray source consists of a sealed transmission x-ray tube with a tungsten anode, producing polychromatic x-rays. A power of 10 W was used with an accelerating voltage of 110 kV. An absorption contrast tomography (ACT) scan was performed to create an absorption mask defining the size and shape of the sample for 3D reconstruction. The sample-to-source distance and sample-to-detector distance were set to 13 mm and 200 mm, respectively. The DCT aperture size was configured to 750×750 μm². During a 360° rotation, 480 diffraction images were collected at 0.75° intervals, with an exposure time of 30 seconds per image, resulting in a total scan duration of approximately four hours. The DCT data was analyzed using GrainMapper3D™. The total reconstructed sample volume was $1095 \times 1095 \times 2920$ μm³ with a voxel size of 5 μm. A minimum misorientation threshold of 0.1° was used to define individual grains. To ensure the accuracy of the reconstructed grains, the LabDCT dataset was filtered using on a minimum grain size of 40 μm, as per the reported limit for the LabDCT[54].

The procedure for aligning the three data sets (Lab-3DXRD, Synch-3DXRD, and LabDCT) comprised two main steps: aligning the orientation of the three data sets via a rigid body rotation ("orientational alignment" in Supplementary Fig. S3b) and aligning the position of the three data sets via a rigid body translation ("translational alignment" in Supplementary Fig. S3b). Both of the 3DXRD datasets were aligned to the LabDCT dataset using the following procedure: (1) First, we identified the five largest grains in each data set. (2) Among these five grains, for each potential grain pair combination, we calculated a rotation that would take the orientation of the 3DXRD grain to the orientation of the LabDCT grain. This yielded $5^2 = 25$ potential rotations based on the possible grain pair combinations. (3) We applied each potential rotation to all grains in the 3DXRD dataset. For each potential rotation, we calculated misorientation, the product of the inverse orientation of one grain with the orientation of the other, between each grain in the 3DXRD dataset and the closest grain in the LabDCT dataset (closest meaning minimum misorientation, in this instance). The rotation that yielded the lowest average misorientation value was selected. (4) To further refine the rotational alignment between the 3DXRD and LabDCT datasets, a fine adjustment with a small extra rotation was determined based on further minimizing the average misorientation value. Grains with misorientation values below 0.25° among the rotated grains were paired. (5) Using the rotationally-aligned grain pairs resulting from Step 4, the 3DXRD grains were translated to match the LabDCT grains. The translation correction was selected as the one that minimized the distances between the paired grain centroids. (6) To further refine the translational alignment between the 3DXRD and LabDCT datasets, a fine adjustment with a small extra translation was determined based on minimizing the average centroid distances. After this step, the grain pair list was re-calculated, this time based on centroid distances below 0.2 mm. A final grain pair list was determined based on misorientation values below 0.25° and centroid distances below 0.2 mm. (7) Steps 1–6 were repeated with different initial grains (rotations) selected in the first step to eliminate any bias errors.

Following dataset alignment, we used only grains that are located within the illuminated volume that is common to all three data sets. This resulted in a $1 \times 1 \times 1$ mm³ volume for the benchmarking validation study. We investigated the parameters associated with the paired grains, i.e., the grain centroids, grain-averaged elastic strain tensors, grain-averaged crystallographic orientations, and relative grain volumes. Through careful comparison and examination of the differences and distributions observed in these measurements, we comprehensively characterize and validate the Lab-3DXRD technique.

Reporting summary

Further information on research design is available in the Nature Portfolio Reporting Summary linked to this article.

Data availability

The datasets generated during the current study are available from the corresponding author on request.

Code availability

The codes used for background removal and preprocessing of acquired images is freely available for download at https://github.com/seungheeAoh/lab3Dxrd.

References

1. Margulies, L., Winther, G. & Poulsen, H. In situ measurement of grain rotation during deformation of polycrystals. *Science* **291**, 2392–2394 (2001).
2. Peng, X., et al. Comparison of simulated and measured grain volume changes during grain growth. *Phys. Rev. Mater.* **6**, 033402 (2022).
3. Bhattacharya, A. et al. Grain boundary velocity and curvature are not correlated in Ni polycrystals. *Science* **374**, 189–193 (2021).
4. Offerman, S. et al. Grain nucleation and growth during phase transformations. *Science* **298**, 1003–1005 (2002).
5. Lauridsen, E. M., Poulsen, H. F., Nielsen, S. F. & Juul Jensen, D. Recrystallization kinetics of individual bulk grains in 90% cold-rolled aluminium. *Acta Materialia* **51**, 4423–4435 (2003).
6. Roumina, R., et al. The dynamics of recrystallized grains during static recrystallization in a hot-compressed Mg-3.2Zn-0.1Ca wt.% alloy using in-situ far field high-energy diffraction microscopy. *Acta Materialia* **234**, 118039 (2022).
7. Gordon, J. V., et al. Evaluating the grain-scale deformation behavior of a single-phase FCC high entropy alloy using synchrotron high energy diffraction microscopy. *Acta Materialia* **215**, 118039 (2021).
8. Schuren, J. C. et al. New opportunities for quantitative tracking of polycrystal responses in three dimensions. *Curr. Opin. Solid State Mater. Sci.* **19**, 235–244 (2015).

9. Abdolvand, H. et al. On the deformation twinning of Mg AZ31B: A three-dimensional synchrotron X-ray diffraction experiment and crystal plasticity finite element model. *Int. J. Plasticity* **70**, 77–97 (2015).
10. Pokharel, R. et al. In-situ observation of bulk 3D grain evolution during plastic deformation in polycrystalline Cu. *Int. J. Plasticity* **67**, 217–234 (2015).
11. Pagan, D. C. et al. Modeling slip system strength evolution in Ti-7Al informed by in-situ grain stress measurements. *Acta Materialia* **128**, 406–417 (2017).
12. Pagan, D. C., Nygren, K. E. & Miller, M. P. Analysis of a three-dimensional slip field in a hexagonal Ti alloy from in-situ high-energy X-ray diffraction microscopy data. *Acta Materialia* **221**, 117372 (2021).
13. Sedmák, P. et al. Grain-resolved analysis of localized deformation in nickel-titanium wire under tensile load. *Science* **353**, 559–562 (2016).
14. Bucsek, A. N. et al. Ferroelastic twin reorientation mechanisms in shape memory alloys elucidated with 3D X-ray microscopy. *J. Mech. Phys. Solids* **124**, 897–928 (2019).
15. Wang, L. et al. Mechanical twinning and detwinning in pure Ti during loading and unloading – an in situ high-energy X-ray diffraction microscopy study. *Scr. Materialia* **92**, 35–38 (2014).
16. Bucsek, A. N. et al. Three-dimensional in situ characterization of phase transformation induced austenite grain refinement in nickel-titanium. *Scr. Materialia* **162**, 361–366 (2019).
17. Li, W. et al. 3D in-situ characterization of dislocation density in nickel-titanium shape memory alloys using high-energy diffraction microscopy. *Acta Materialia* **266**, 119659 (2024).
18. Worsnop, F. F. et al. The influence of alloying on slip intermittency and the implications for dwell fatigue in titanium. *Nat. Commun.* **13**, 5949 (2022).
19. Lim, R. E., Pagan, D. C., Bernier, J. V., Shade, P. A. & Rollett, A. D. Grain reorientation and stress-state evolution during cyclic loading of an α -Ti alloy below the elastic limit. *Int. J. Fatigue* **156**, 106614 (2022).
20. Naragani, D. P., Shade, P. A., Kenesei, P., Sharma, H. & Sangid, M. D. X-ray characterization of the micromechanical response ahead of a propagating small fatigue crack in a Ni-based superalloy. *Acta Materialia* **179**, 342–359 (2019).
21. Spear, A. D., Li, S. F., Lind, J. F., Suter, R. M. & Ingraffea, A. R. Three-dimensional characterization of microstructurally small fatigue-crack evolution using quantitative fractography combined with post-mortem X-ray tomography and high-energy X-ray diffraction microscopy. *Acta Materialia* **76**, 413–424 (2014).
22. Maloth, T. et al. Multiscale modeling of cruciform dwell tests with the uncertainty-quantified parametrically homogenized constitutive model. *Acta Materialia* **200**, 893–907 (2020).
23. Hanson, J. P. et al. Crystallographic character of grain boundaries resistant to hydrogen-assisted fracture in Ni-base alloy 725. *Nat. Commun.* **9**, 3386 (2018).
24. Rovinelli, A., Sangid, M. D., Proudhon, H. & Ludwig, W. Using machine learning and a data-driven approach to identify the small fatigue crack driving force in polycrystalline materials. *npj Computational Mater.* **4**, 35 (2018).
25. Gustafson, S. et al. Quantifying microscale drivers for fatigue failure via coupled synchrotron X-ray characterization and simulations. *Nat. Commun.* **11**, 3189 (2020).
26. Naragani, D. et al. Investigation of fatigue crack initiation from a non-metallic inclusion via high energy x-ray diffraction microscopy. *Acta Materialia* **137**, 71–84 (2017).
27. Poulsen, H. F., Margulies, L., Schmidt, S. & Winther, G. Lattice rotations of individual bulk grains. *Acta Materialia* **51**, 3821–3830 (2003).
28. Suter, R. M., Hennessy, D., Xiao, C. & Lienert, U. Forward modeling method for microstructure reconstruction using x-ray diffraction microscopy: single-crystal verification. *Rev. Sci. Instrum.* **77**, 123905 (2006).
29. Lim, R. E. et al. Grain-resolved temperature-dependent anisotropy in hexagonal Ti-7Al revealed by synchrotron X-ray diffraction. *Mater. Charact.* **174**, 110943 (2021).
30. Zhang, X. et al. High-energy x-ray diffraction microscopy study of deformation microstructures in neutron-irradiated polycrystalline Fe-9%Cr. *J. Nucl. Mater.* **508**, 556–566 (2018).
31. Sparks, G. et al. 3D Reconstruction of a High-Energy Diffraction Microscopy Sample Using Multi-modal Serial Sectioning with High-Precision EBSD and Surface Profilometry. *Integr. Mater. Manuf. Innov.* **13**, 773–803 (2024).
32. Web of Science. *2004-2023 Times Cited, Journal Citation Reports (Clarivate, 2024)*.
33. Li, W. et al. Resolving intragranular stress fields in plastically deformed titanium using point-focused high-energy diffraction microscopy. *J. Mater. Res.* **38**, 165–178 (2023).
34. Hayashi, Y., Setoyama, D., Hirose, Y., Yoshida, T. & Kimura, H. Intragranular three-dimensional stress tensor fields in plastically deformed polycrystals. *Science* **366**, 1492–1496 (2019).
35. Henningsson, N. A., Hall, S. A., Wright, J. P. & Hektor, J. Reconstructing intragranular strain fields in polycrystalline materials from scanning 3DXRD data. *J. Appl. Crystallogr.* **53**, 314–325 (2020).
36. Park, J. -S. et al. Far-field high-energy diffraction microscopy: a non-destructive tool for characterizing the microstructure and micromechanical state of polycrystalline materials. *Micros. Today* **25**, 36–45 (2017).
37. Quey, R., Dawson, P. R. & Barbe, F. Large-scale 3D random polycrystals for the finite element method: generation, meshing and remeshing. *Computer Methods Appl. Mech. Eng.* **200**, 1729–1745 (2011).
38. Park, J. -S. et al. High-energy synchrotron x-ray techniques for studying irradiated materials. *J. Mater. Res.* **30**, 1380–1391 (2015).
39. Joel B. et al. HEXRD/hexrd: Release 0.9.3. Zenodo https://doi.org/10.5281/ZENODO.8033940 (2023).
40. Wright, J. FABLE-3DXRD/ImageD11. https://github.com/FABLE-3DXRD/ImageD11.
41. Wang, L. et al. Evaluating the Taylor hardening model in polycrystalline Ti using high energy X-ray diffraction microscopy. *Scr. Materialia* **195**, 113743 (2021).
42. Pagan, D. C. & Miller, M. P. Determining heterogeneous slip activity on multiple slip systems from single crystal orientation pole figures. *Acta Materialia* **116**, 200–211 (2016).
43. Nygren, K. E., Pagan, D. C., Bernier, J. V. & Miller, M. P. An algorithm for resolving intragranular orientation fields using coupled far-field and near-field high energy X-ray diffraction microscopy. *Mater. Charact.* **165**, 110366 (2020).
44. Greeley, D. A., Adams, J. F., Kenesei, P., Spear, A. D. & Allison, J. E. Quantitative analysis of three-dimensional fatigue crack path selection in Mg alloy WE43 using high-energy X-ray diffraction microscopy. *Fatigue Fract. Eng. Mat. Struct.* **47**, 1150–1171 (2024).
45. Bucsek, A. N., Dale, D., Ko, J. Y. P., Chumlyakov, Y. & Stebner, A. P. Measuring stress-induced martensite microstructures using far-field high-energy diffraction microscopy. *Acta Crystallogr A Found. Adv.* **74**, 425–446 (2018).
46. Thibault, P. & Elser, V. X-ray diffraction microscopy. *Annu. Rev. Condens. Matter Phys.* **1**, 237–255 (2010).
47. Lee, M. et al. *X-Ray Diffraction for Materials Research: From Fundamentals to Applications*. (Apple Academic Press, Oakville, ON, Canada; Waretown, NJ, USA, 2016).
48. Warren, B. E. et al. *X-Ray Diffraction*. (Dover Publications, New York, 1990).

49. King, A., Johnson, G., Engelberg, D., Ludwig, W. & Marrow, J. Observations of intergranular stress corrosion cracking in a grain-mapped polycrystal. *Science* **321**, 382–385 (2008).
50. Ludwig, W., Schmidt, S., Lauridsen, E. M. & Poulsen, H. F. X-ray diffraction contrast tomography: a novel technique for three-dimensional grain mapping of polycrystals. I. direct beam case. *J. Appl Crystallogr* **41**, 302–309 (2008).
51. Reischig, P. et al. Advances in X-ray diffraction contrast tomography: flexibility in the setup geometry and application to multiphase materials. *J. Appl Crystallogr* **46**, 297–311 (2013).
52. McDonald, S. A. et al. Non-destructive mapping of grain orientations in 3D by laboratory X-ray microscopy. *Sci. Rep.* **5**, (2015). 14665.
53. Bachmann, F., Bale, H., Gueninchault, N., Holzner, C. & Lauridsen, E. M. 3D grain reconstruction from laboratory diffraction contrast tomography. *J. Appl Crystallogr* **52**, 643–651 (2019).
54. McDonald, S. A. et al. Tracking polycrystal evolution non-destructively in 3D by laboratory X-ray diffraction contrast tomography. *Mater. Charact.* **172**, 110814 (2021).
55. Zhao, Y., Niverty, S., Ma, X. & Chawla, N. Correlation between corrosion behavior and grain boundary characteristics of a 6061 Al alloy by lab-scale X-ray diffraction contrast tomography (DCT). *Mater. Charact.* **193**, 112325 (2022).
56. Sirdesai, N. N., Singh, T. N. & Pathegama Gamage, R. Thermal alterations in the poro-mechanical characteristic of an Indian sandstone – a comparative study. *Eng. Geol.* **226**, 208–220 (2017).
57. Li, T., Senesi, A. J. & Lee, B. Small Angle X-ray Scattering for Nanoparticle Research. *Chem. Rev.* **116**, 11128–11180 (2016).
58. Koch, M. H. J. SAXS Instrumentation for Synchrotron Radiation then and now. *J. Phys.: Conf. Ser.* **247**, 012001 (2010).
59. Ilavsky, J. et al. Ultra-small-angle X-ray scattering at the Advanced Photon Source. *J. Appl Crystallogr* **42**, 469–479 (2009).
60. Hexemer, A. & Müller-Buschbaum, P. Advanced grazing-incidence techniques for modern soft-matter materials analysis. *IUCrJ* **2**, 106–125 (2015).
61. Gräwert, T. W. & Svergun, D. I. Structural Modeling Using Solution Small-Angle X-ray Scattering (SAXS). *J. Mol. Biol.* **432**, 3078–3092 (2020).
62. Xiong, B., Chen, R., Zeng, F., Kang, J. & Men, Y. Thermal shrinkage and microscopic shutdown mechanism of polypropylene separator for lithium-ion battery: In-situ ultra-small angle X-ray scattering study. *J. Membr. Sci.* **545**, 213–220 (2018).
63. Kikhney, A. G. & Svergun, D. I. A practical guide to small angle X-ray scattering (SAXS) of flexible and intrinsically disordered proteins. *FEBS Lett.* **589**, 2570–2577 (2015).
64. Bolze, J. & Gateshki, M. Highly versatile laboratory X-ray scattering instrument enabling (nano-)material structure analysis on multiple length scales by covering a scattering vector range of almost five decades. *Rev. Sci. Instrum.* **90**, 123103 (2019).
65. Bernier, J. V., Suter, R. M., Rollett, A. D. & Almer, J. D. High-Energy X-Ray Diffraction Microscopy in Materials Science. *Annu. Rev. Mater. Res.* **50**, 395–436 (2020).
66. Ganju, E., Nieto-Valeiras, E., LLorca, J. & Chawla, N. A novel diffraction contrast tomography (DCT) acquisition strategy for capturing the 3D crystallographic structure of pure titanium. *Tomogr. Mater. Struct.* **1**, 100003 (2023).
67. Greeley, D. A. et al. Quantitative three-dimensional investigation of cyclic deformation mechanisms in Mg Alloys. https://doi.org/10.7302/8163 (2023).
68. Fang, H., Ludwig, W. & Lhuissier, P. Reconstruction algorithms for grain mapping by laboratory X-ray diffraction contrast tomography. *J. Appl Crystallogr* **55**, 1652–1663 (2022).
69. Chen, Z. P. et al. Enhancing the signal-to-noise ratio of x-ray diffraction profiles by smoothed principal component analysis. *Anal. Chem.* **77**, 6563–6570 (2005).
70. Martin, A. V. et al. Noise-robust coherent diffractive imaging with a single diffraction pattern. *Opt. Express* **20**, 16650 (2012).
71. Larsson, D. H., Takman, P. A. C., Lundström, U., Burvall, A. & Hertz, H. M. A 24 keV liquid-metal-jet x-ray source for biomedical applications. *Rev. Sci. Instrum.* **82**, 123701 (2011).
72. Lechowski, B. et al. Laboratory X-ray Microscopy of 3D Nanostructures in the Hard X-ray Regime Enabled by a Combination of Multilayer X-ray Optics. *Nanomaterials* **14**, 233 (2024).
73. Moy, J.-P. Large area X-ray detectors based on amorphous silicon technology. *Thin Solid Films* **337**, 213–221 (1999).
74. Kuttig, J. D. et al. Comparative investigation of the detective quantum efficiency of direct and indirect conversion detector technologies in dedicated breast CT. *Phys. Med.* **31**, 406–413 (2015).
75. Datta, A., Fiala, J. & Motakef, S. 2D perovskite-based high spatial resolution X-ray detectors. *Sci. Rep.* **11**, 22897 (2021).
76. Bernier, J. V., Barton, N. R., Lienert, U. & Miller, M. P. Far-field high-energy diffraction microscopy: a tool for intergranular orientation and strain analysis. *J. Strain Anal. Eng. Des.* **46**, 527–547 (2011).
77. González, A. et al. 1.5 *Comprehensive Biophysics* Ch1.5 X-Ray Crystallography: Data Collection Strategies and Resources. (Elsevier, 2012).

Acknowledgements

This work is supported by the National Science Foundation under award CMMI-2142302 and the U.S. Department of Energy Office of Basic Energy Sciences Division of Materials Science and Engineering under Award DE-SC0008637 as part of the Center for PRedictive Integrated Structural Materials Science (PRISMS). This work also includes research conducted at the Center for High-Energy X-ray Sciences (CHEXS), which is supported by the National Science Foundation (BIO, ENG and MPS Directorates) under award DMR-1829070. The authors acknowledge the University of Michigan College of Engineering for financial support and the Michigan Center for Materials Characterization for use of the instruments and staff assistance. SO and AB also thank Dr. Rachel Lim at Lawrence Livermore National Laboratory for her help with the HEXRD software package.

Author contributions

Conceptualization: S.O., A.B., Methodology: S.O., Y.J., S.L., K.G., M.W., R.D., Investigation: S.O., W.L., Supervision: A.B., Writing – original draft: S.O., W.L., A.B.

Competing interests

The authors declare no competing interests.

Additional information

Supplementary information The online version contains supplementary material available at https://doi.org/10.1038/s41467-025-58255-x.

Correspondence and requests for materials should be addressed to Seunghee Oh or Ashley Bucsek.

Peer review information *Nature Communications* thanks the anonymous reviewer(s) for their contribution to the peer review of this work. A peer review file is available.